Resonating valence bond trial wave functions with both static and dynamically determined Marshall sign structure

Xiaoming Zhang[1,2,3] and K. S. D. Beach[1,*]

[1]*Department of Physics, University of Alberta, Edmonton, Alberta, Canada T6G 2E1*

[2]*Department of Physics and Astronomy, University of Western Ontario, London, Ontario, Canada N6A 3K7*

[3]*Department of Earth Sciences, University of Western Ontario, London, Ontario, Canada N6A 5B7*

(Received 4 October 2012; revised manuscript received 21 February 2013; published 20 March 2013)

We construct energy-optimized resonating valence bond wave functions as a means to sketch out the zero-temperature phase diagram of the square-lattice quantum Heisenberg model with competing nearest- (J_1) and next-nearest-neighbor (J_2) interactions. Our emphasis is not on achieving an accurate representation of the magnetically disordered intermediate phase (centered on a relative coupling $g = J_2/J_1 \sim \frac{1}{2}$ and whose exact nature is still controversial) but on exploring whether and how the Marshall sign structure breaks down in the vicinity of the phase boundaries. Numerical evaluation of two- and four-spin correlation functions is carried out stochastically using a worm algorithm that has been modified to operate in either of two modes: one in which the sublattice labeling is fixed beforehand and another in which the worm manipulates the current labeling so as to sample various sign conventions. Our results suggest that the disordered phase evolves continuously out of the (π,π) Néel phase and largely inherits its Marshall sign structure; on the other hand, the transition from the magnetically ordered $(\pi,0)$ phase is strongly first order and involves an abrupt change in the sign structure and spatial symmetry as the result of a level crossing.

DOI: 10.1103/PhysRevB.87.094420 PACS number(s): 75.10.Jm, 75.10.Kt, 05.30.Rt, 75.30.Kz

I. INTRODUCTION

Simple spin models have contributed significantly to our understanding of quantum magnetism. They consist of mutually interacting spin-S objects arranged in a lattice and are meant to describe the behavior of localized electrons in a crystalline environment. Such models are generally viewed as effective, low-energy descriptions, descended from their electronic parent models by a process of integrating out the gapped charge degrees of freedom.[1]

A tremendous variety of spin interactions can arise. In particular, a "t/U"-style power series from the strong correlation limit generates (or at least motivates) an increasingly complicated zoo of multispin interaction terms.[2–6] Nonetheless, we know that even the leading-order term in the expansion, corresponding to Heisenberg models with just two-spin interactions, can display highly nontrivial physics if the exchange interactions are sufficiently frustrating.[7,8] In that case, the ground state may be a magnetically disordered, spin-rotation-invariant state (either liquid[9] or solid[10,11]) having no classical analog.

Otherwise, conventional magnetic order (at some ordering vector $\mathbf{Q}$) is a generic feature of the ground state for Heisenberg models in spatial dimension greater than one.[12,13] The absence of frustration is connected to three inter-related properties: (i) the existence of a bipartite labeling such that all antiferromagnetic interactions connect sites in opposite sublattices, (ii) strict adherence to a Marshall sign rule,[14] and (iii) the possibility of transforming mechanistically to a basis in which all amplitudes of the wave function are real and non-negative. The last of these is why nonfrustrated models can be easily simulated using quantum Monte Carlo approaches.[15–17]

For the $S = \frac{1}{2}$ case, all three properties are conceptually unified in the language of *valence bonds*.[18–22] The collinear, $\mathbf{Q}$-ordered ground state of a nonfrustrated Heisenberg model can be described in a bipartite valence bond basis[22,23] in which the AB sublattice labeling coincides with the alternating pattern laid out by $\mathbf{Q}$ and only spins in opposite sublattices are bound into singlet pairs. In terms of such a basis $\mathcal{V}_{\mathrm{AB}} = \{|v\rangle\}$, the ground state has an expansion $|\psi\rangle = \sum_v \psi(v)|v\rangle$ in which each amplitude $\psi(v)$ is real and non-negative. The exact amplitudes can be obtained numerically by projection.[24–28]

It is also possible to find extremely good approximate values of the form $\psi(v) \approx \prod_{[i,j]\in v} h(\mathbf{r}_{ij})$, where $h(\mathbf{r}) > 0$ is a function of the vector connecting bond endpoints. This resonating valence bond (RVB) ansatz, due to Liang, Doucot, and Anderson,[29] strictly enforces the geometric tiling constraint on the singlet bonds but ignores additional bond-bond correlations.[30] For a magnetically ordered state, one can show that factorizability into individual bond amplitudes is the correct assumption.[31,32] Moreover, for nonfrustrated systems, the amplitudes exhibit power-law decay, and hence the wave function contains bonds on all length scales.

As a specific and illustrative example, we consider the square-lattice J_1-J_2 model for spin half. It has two nonfrustrated limits. The model with anitferromagnetic nearest-neighbor interactions only ($J_1 = 1$, $J_2 = 0$) exhibits a Néel ordered ground state whose staggered moment is roughly 60% of its fully polarized, classical value. The state is almost perfectly captured by an RVB wave function whose bond amplitudes are computed as $h(\mathbf{r}) = \sum_{\mathbf{q}} e^{i\mathbf{q}\cdot\mathbf{r}}\left[1 - (1-\gamma_{\mathbf{q}}^2)^{1/2}\right]/\gamma_{\mathbf{q}}$. Here, $\gamma_{\mathbf{q}} = (\cos q_x + \cos q_y)/2$, and the wave-vector sum is taken over a Brillouin zone reduced with respect to $\mathbf{Q} = (\pi,\pi)$. The opposite limit, with *next*-nearest-neighbor interactions dominating ($J_1 = 0^+$, $J_2 = 1$), is equivalent to two interpenetrating nearest-neighbor Heisenberg antiferromagnets rotated 45°. The spin directions in the two otherwise disjoint subsystems lock to each other[33] provided that J_1 is not strictly zero. In this case, the ground state is equally well described by the RVB wave function, but with the substitution of $\gamma_{\mathbf{q}} = \cos q_x \cos q_y$ and a Brillouin zone defined modulo $\mathbf{Q} = (\pi,0)$ or $\mathbf{Q} = (0,\pi)$.

What we present in this paper is an attempt to interpolate between these two limits (through the entire range of relative couplings that are highly frustrated) using the RVB state as a variational wave function. Our approach is inspired by Ref. 34, but there are several important differences. The first is simply the scale of the calculation: we have simulated a large number of lattice sizes up to $L = 32$ on a dense grid of relative coupling values ($g = J_2/J_1$ ranging from 0 to 1 in steps of $\delta g = 0.01$). Second, we do not require that $h(\mathbf{r})$ respect the full C_4 symmetry of the square lattice. Rather, we impose only the x- and y-axis reflection symmetry, giving the amplitudes an opportunity either to acquire (over the course of the energy optimization) the full symmetry or to settle into a state that looks different under 90° rotation. Third, we explore the space of AB sublattice labelings by which the bipartite valence bond basis is constructed.

As in Ref. 34, we make use of an unbiased, stochastic optimization scheme. Changes to the $h(\mathbf{r})$ values are made in the downhill direction of the local energy gradient. Step sizes are randomized, and their magnitude decreases on a power-law schedule. We do not attempt to guide the optimization, other than to ensure that none of the bond amplitudes goes negative; nor do we impose any constraints on the variational parameters based on any prior knowledge (gleaned, e.g., from mean-field theory[31] or from a master-equation analysis[35]).

We discover the following. At this level of approximation, the J_1-J_2 model does indeed support a magnetically disordered intermediate phase. But, its width is much smaller than expected: the phase boundaries are found to be at $g_{c1} \doteq 0.54(1)$ and $g_{c2} \doteq 0.5891(3)$. The transitions are unambiguously second and first order, respectively, with the ground state achieving the full C_4 symmetry for all $g < g_{c2}$. As the system is tuned up from $g = 0$, increasing frustration eventually extinguishes the (π,π) ordered moment at g_{c1} in a continuous fashion.

The disappearance of magnetic order is preceded by a failure of the Marshall sign rule at $g_{M1} \doteq 0.398(4)$, in agreement with the scenario first outlined by Richter and co-workers.[36] Still, even though the rule is not strictly obeyed beyond g_{M1}, the Marshall structure inherited from the $g = 0$ model remains largely intact throughout the intermediate phase. This is true in the sense that continuing to define the bipartite bond basis from a *checkerboard* sublattice decomposition produces only a microscopic number of negative $h(\mathbf{r})$ values: only $h(\pm1,\pm2)$ and $h(\pm2,\pm1)$ initially. Moreover, when we allow the AB pattern to arise on its own within the simulation (described in detail in Secs. II D and III), the checkerboard pattern is the one selected whenever $g < g_{c2}$.

On the other hand, the RVB state at large g explicitly breaks the 90° rotation symmetry and has a Marshall sign structure based on a *stripe* sublattice decomposition. As the coupling is tuned down from the $g = \infty$ limit, the $(\pi,0)$ ordered moment is not strongly affected, and it persists with only weak variation (never dropping below 47% of its fully polarized value) down to g_{c2}, where the spatially symmetric, checkerboard-based RVB wave function takes over as the lowest-energy state. This state in the region $g_{c1} < g < g_{c2}$ is, as far as we can tell, featureless. It exhibits no long-range spin or dimer order, and it breaks no symmetries. It is not, however, a "short-range RVB state" in the usual sense since it is not made up of predominantly short bonds. Its amplitude function $h(\mathbf{r})$ is highly anisotropic (as anticipated elsewhere[35]) and remains long ranged along the principal spatial axes. Spin correlations appear to be critical and to display circular symmetry at long distances, despite the anisotropy of the bond weights. Dimer correlations decay either exponentially or with a high power law. This is in stark contrast to the usual short-bond-only RVB state, often referred to as the nearest-neighbor RVB (NNRVB), which has spin correlations that decay exponentially[29] and dimer correlations that decay algebraically.[37,38] Moreover, the presence of long bonds implies an absence of the topological order[37,38] that is characteristic of a purely short-ranged RVB state in two dimensions.

II. MODEL AND METHOD

A. Frustrated Hamiltonian

The spin-half, square-lattice Heisenberg model with frustrating interactions has a Hamiltonian

$$H = J_1 \sum_{\langle i,j \rangle} \mathbf{S}_i \cdot \mathbf{S}_j + J_2 \sum_{\langle\langle i,j \rangle\rangle} \mathbf{S}_i \cdot \mathbf{S}_j, \tag{1}$$

where $J_1 > 0$ and $J_2 > 0$ are the antiferromagnetic exchange couplings. The summations range over pairs of adjacent sites $\langle i,j \rangle$ and over farther pairs $\langle\langle i,j \rangle\rangle$ that sit diagonally across a plaquette. The ratio $g = J_2/J_1$ is the key tuning parameter at zero temperature. In the classical version of this model ($S \to \infty$), two magnetic phases meet at exactly $g = 0.5$, separated by a first-order transition.[39–42]

In the $S = \frac{1}{2}$ problem, the two magnetically ordered ground states obtain for values $g \lesssim 0.4$ and $g \gtrsim 0.6$,[43–48] and a magnetically disordered phase intervenes. (There is, however, a good deal of disagreement over the exact positions of the critical points; cf. Refs. 49 and 50, which put the lower critical point as low as 0.35 and as high as 0.45.) The physics of the phase in the intermediate region is not known with complete certainty, but it is commonly believed to be short ranged and not to exhibit any kind of conventional magnetic order. One possibility is a crystalline arrangement of valence bonds, a state with broken translational symmetry in which singlet formation favors an enlargement of the unit cell beyond that of the underlying square lattice.[50–63] A featureless spin liquid that does not break any symmetries is another possibility.[64–74]

The case for a spin-liquid ground state has been advanced by recent tensor product[75] and density matrix renormalization group (DMRG)[76] calculations and by a variational approach based on the entangled-plaquette ansatz.[77] With regard to the DMRG result, Sandvik has suggested that the use of a cylindrical geometry complicates the detection of crystalline order.[78] His numerical experiments seem to indicate that the mixture of open and closed boundary conditions significantly raises the crossover length scale ξ beyond which bond order takes hold (i.e., where the finite-size scaling behavior of the dimer-dimer correlations is truly in the asymptotic regime). Such questions are difficult to resolve. Unlike in three-dimensional systems, where crystalline bond order, if it is present, is almost always strong,[5,79] in two dimensions it is quite delicate and can easily be disguised by a U(1) effective symmetry for system sizes $L \lesssim \xi$. (See Secs. III and IV of

Ref. 80 and references therein.) Here, we attempt to make the best of this unsatisfactory state of affairs. We simply take the point of view that, for the lattice sizes (up to $L = 32$) we can simulate, the liquid and the weakly ordered bond crystal are indistinguishable.

B. RVB trial wave function

In quantum Heisenberg models, competing interactions that frustrate the order have the potential to stabilize exotic quantum phases, but they also render the problem computationally intractable on large lattices. Frustrating interactions of even infinitesimal strength cause a sign problem[81] that makes quantum Monte Carlo calculations unfeasible. Moreover, the size of the Hilbert space grows exponentially with system size and is thus beyond the capability of exact diagonalization calculations if we want to get near the thermodynamic limit. (The record for spin-half has recently jumped from 42 sites[49,82–84] to 48 sites,[85] a terribly impressive technical feat that nonetheless limits us to two-dimensional length scales $\sim\sqrt{48}$ that are quite small.) An approximate method based on good trial wave functions is therefore one of the few remaining possibilities for large systems.

We consider a lattice of $2N$ spins and a factorizable RVB wave function of the form

$$|\psi\rangle = \sum_{v} \prod_{[i,j]\in v} h(\mathbf{r}_{ij})|v\rangle, \tag{2}$$

where the sum is over all partitions of the lattice into N directed pairs $v = ([i_1, j_1],[i_2, j_2], \ldots,[i_N, j_N])$. To every such *dimer covering* v, there is a corresponding singlet product state; e.g.,

$$|v\rangle = \frac{1}{2^{N/2}} \bigotimes_{[i,j]\in v} (|\uparrow_i \downarrow_j\rangle - |\downarrow_i \uparrow_j\rangle) \tag{3}$$

in the $S = \frac{1}{2}$ case. The set $\mathcal{V} = \{|v\rangle\}$ of all possible singlet product states is both overcomplete and nonorthogonal and constitutes the so-called valence bond basis.

We can now break up the lattice into two sublattices, groups of sites labeled A and B, equal in number, and restrict ourselves to a reduced basis in which valence bonds connect only sites in opposite sublattices (i.e., $v \in \mathcal{V}_{\mathrm{AB}} \simeq S_N$, rather than $v \in \mathcal{V} \simeq S_{2N}/Z_2^N$). We adopt the convention that each bond $[i, j]$ is arranged with site i in sublattice A and site j in sublattice B. This has the advantage of rendering the overlap strictly positive: $\langle v|v'\rangle = 2^{N_l(C)-N}$, where $N_l(C)$ is the number of loops in the double dimer covering $C = (v, v')$. (In this "bosonic" convention, the singlets are AB directed bonds. In the complementary "fermionic" convention, the bonds are directionless and all signs are moved into the overlaps.[64,86–89])

To start, we consider two families of trial state, each built using a bipartite bond basis consistent with one of two static choices of sublattice labeling, viz., the checkerboard and stripe patterns shown in Fig. 1. Later in the paper, we go on to describe a procedure in which the trial state is built using an unrestricted bond basis and the sublattice labeling (and hence the Marshall sign convention) is determined dynamically.

The RVB wave function is quite expressive. Its degrees of freedom are the full set of $h(\mathbf{r})$ values with the bond vector $\mathbf{r}$ spanning all lengths and orientations that can be achieved on an $L \times L$ cluster with periodic boundary conditions and

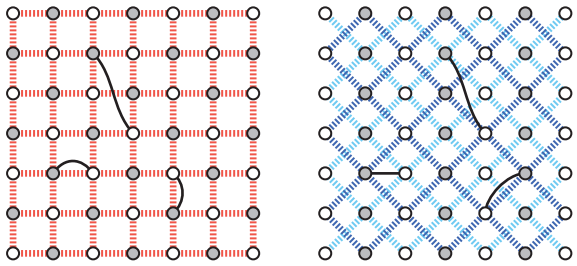

FIG. 1. (Color online) Square grid of lattice sites (circles) whose shading indicates the sublattice membership. Dashed lines mark the J_1 (red) and J_2 (blue) exchange couplings. The basis contains only product states of singlets connecting sites in opposite sublattices. (Left) In the limit $g = J_2/J_1 = 0$, a checkerboard pattern of A and B labels that coincides with (π,π) magnetic order. (Right) In the limit $g = \infty$, a stripe pattern that coincides with $(\pi,0)$ order. In each case, three permissible singlet pairings are indicated.

that are unique up to whatever symmetries are enforced. (Still, the total number of parameters grows only linearly with the number of spins, which is radically slower than the number of states in the total spin singlet sector.) Previous calculations of this kind[34,35] considered only the checkerboard AB pattern and imposed on $h(\mathbf{r}) = h(x, y)$ the full symmetry of the lattice, such that $h(x, y) = h(|x|,|y|) = h(|y|,|x|)$. In this calculation, we impose a less restrictive condition $h(x, y) = h(|x|,|y|)$ that respects reflection symmetry across the lines $x = 0$ and $y = 0$ but not across the lines $y = \pm x$. For the checkerboard pattern, the number of free parameters is $(L/2 - \eta)(L/2 - 1)$, where $\eta = (L/2 \bmod 2)$ distinguishes between $L/2$ even and odd. For the stripe pattern, the count is only slightly higher: $(L/2 + 1)(L/2 - 1) = L^2/4 - 1$.

To recapitulate, our work involves a basis choice. We do not construct the trial wave functions from the largest possible set of valence bond states in which the spins are joined in all possible ways. Instead, we obtain a more restricted basis by dividing the system into two groups of sites (A and B) and keeping only states in which bonds connect A sites and B sites (bipartite bonds). No approximation is involved in this basis choice since the restricted basis is so massively overcomplete that even this subset still spans the relevant part of the Hilbert space.

But in assigning A and B labels to the sites, we are making a choice about the form of the trial wave function. By working with the checkerboard and stripe AB patterns, we are in essence adapting the trial wave function to $g = 0$ and ∞, respectively, and taking advantage of the Marshall sign rules that exist in those two limits. We are not biasing the wave function, however, at least not in the sense that we are building in magnetic order. The wave functions constructed from either AB pattern are fully capable of representing nonmagnetic states.

C. Sampling algorithm

Every measurement $\langle\hat{O}\rangle = \langle\psi|\hat{O}|\psi\rangle/\langle\psi|\psi\rangle$ is equivalent to $\langle\langle O\rangle\rangle$, an ensemble average of the appropriate estimator $O : C \to O(C)$ in the gas of fluctuating loops described by

$$Z = \frac{1}{q^N} \sum_{C} q^{N_l(C)} \prod_{[i,j]\in C} h_{ij}. \tag{4}$$

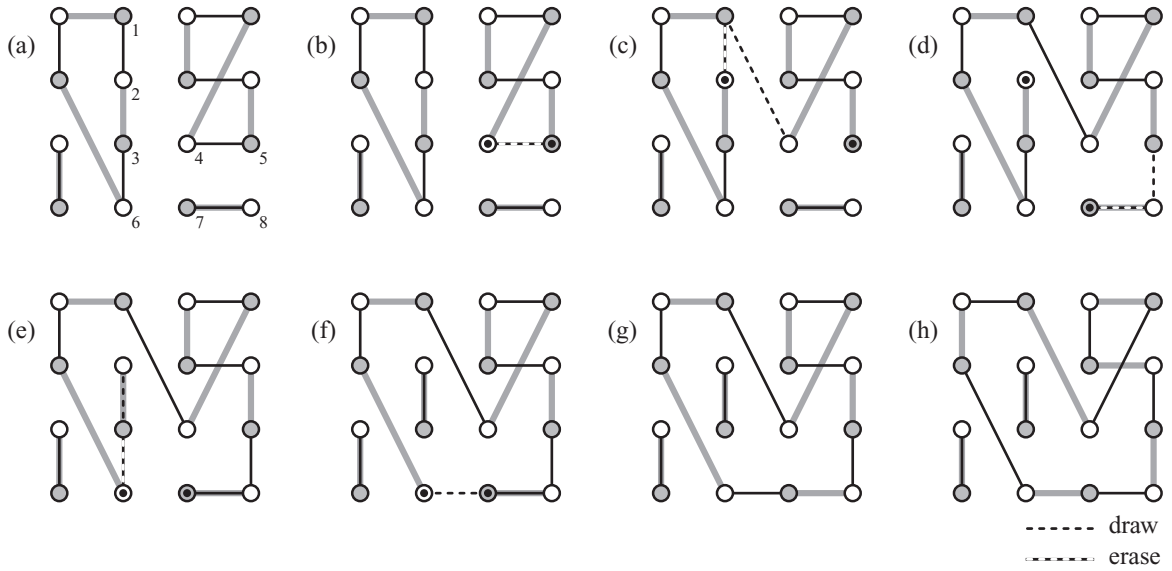

FIG. 2. (a) Two superimposed valence bond configurations form a collection of closed loops. Eight of the sites are numbered for use in Eq. (6). (b) Breaking one bond leaves an open string with a head and tail located at the former bond's endpoints. (c)–(e) The head and tail move by drawing a new bond and erasing the preexisting bond emerging from the destination site. (f) The open string is closed when the head and tail reconnect. (g) The repaired loop configuration. (h) Exchanging the background and foreground links in any loop is also a valid update.

As before, $C = (v, v')$ is a loop configuration arising from the superposition of two dimer coverings, and $N_l(C)$ counts the number of loops. The value $q = 2$ is the loop fugacity appropriate for $S = \frac{1}{2}$. When Marshall's theorem holds, the bond amplitudes satisfy $h_{ij} \geqslant 0$ and thus every term in Eq. (4) is non-negative. This model is amenable to Monte Carlo simulation. We now outline a simple and efficient algorithm for performing the stochastic sampling.

As a formal trick (in the spirit of Ref. 90), we enlarge the phase space from Φ_0 to $\Phi_0 \times \Phi_1 \times \cdots \times \Phi_N$, where Φ_n is the set of configurations in which $2n$ free endpoints have been introduced by breaking n valence bonds. (The system has been converted to one of both closed loops and open strings.) We take the partition function to be

$$Z = \frac{1}{q^N} \sum_C q^{N_l(C)} \sigma^{N_s(C)} \prod_{[i,j]\in C} h_{ij}. \tag{5}$$

The configurations C are now assembled from all possible partial coverings $v = ([i_1, j_1], [i_2, j_2], \ldots, [i_n, j_n])$ of variable length $0 \leqslant n \leqslant N$, and σ is introduced as a fugacity for the open strings [numbering $N_s(C) = N - n$]. The loop-only sector corresponds to the original partition function $Z_0 = \langle 1 \rangle_{\Phi_0}$. (In each string sector, there is a Green's function defined by the string endpoints: $G_{ij} = \langle \delta_{i,\alpha_1} \delta_{j,\beta_1} \rangle_{\Phi_1}$, $G_{ij;kl} = \langle \delta_{i,\alpha_1} \delta_{j,\beta_1} \delta_{k,\alpha_2} \delta_{l,\beta_2} \rangle_{\Phi_2}$, etc. Here, α_n and β_n denote the positions of the head and tail of the nth string. It is worth emphasizing that these $2n$-point Green's functions do not coincide with expectation values of the physical spin operators. In general, we must take all measurements in the Φ_0 configuration space using the loop estimators derived in Ref. 22.)

We will consider a process that involves breaking a single valence bond ($\Phi_0 \to \Phi_1$) to produce an open string whose two endpoints (the "head" and "tail") serve as walkers subject to Monte Carlo updates. The walkers move via a series of two-step motions that involve drawing a new bond and erasing an old one. When the walkers meet, the loop is closed ($\Phi_1 \to \Phi_0$). Figure 2 shows an example circuit. The fives successive steps shown in Figs. 2(b)–2(f) produce an overall change in the relative weight

$$\frac{\sigma}{h_{5,4}} \times \frac{h_{1,4}}{q h_{1,2}} \times \frac{h_{5,8}}{q h_{7,8}} \times \frac{q h_{3,2}}{h_{3,6}} \times \frac{h_{7,6}}{\sigma}. \tag{6}$$

Since we have chosen the bond amplitudes h_{ij} to be non-negative, we can define a local amplitude $H_i = \sum_j h_{ij}$ and a total overall amplitude $\mathsf{H} = \sum_i H_i = \sum_{ij} h_{ij}$. These definitions will be useful in the derivations that follow.

To begin, let us consider processes that take the system from the space of loops to the space of loops and one string. We move from a configuration $C \sim [i, j]$ to a configuration $C' \sim (i)(j)$ by breaking a bond $[i, j]$ and thus leaving string endpoints (i) and (j). The transition probabilities for breaking and repairing the bond obey the detailed balance equation

$$W^{\text{break}}_{[i,j]} P(i) \pi_C = W^{\text{repair}}_{(i)(j)} P(j|i) \pi_{C'}. \tag{7}$$

Here, $P(i)$ is the probability of choosing a site i whose bond we want to break, and $P(j|i)$ is the probability of choosing j given a walker (string endpoint) at site i. π_C and $\pi_{C'}$ represent the likelihood of the system being found in configurations C and C'. Their ratio is given by

$$\frac{\pi_{C'}}{\pi_C} = \frac{\sigma}{h_{ij}}. \tag{8}$$

If we choose which bond to break according to the distribution of local bond weight $P(i) = H_i/\mathsf{H}$ and choose walker movements according to the distribution $P(j|i) = h_{ij}/H_i$, then

$$\delta = \frac{W^{\text{break}}_{[i,j]}}{W^{\text{repair}}_{(i)(j)}} = \frac{P(j|i)\pi_{C'}}{P(i)\pi_C} = \frac{\sigma}{\mathsf{H}}. \tag{9}$$

We are free to choose $\sigma = \mathsf{H}$, in which case the transition probabilities $W^{\text{break}}_{[i,j]}$ and $W^{\text{repair}}_{(i)(j)}$ are equal and unit valued.

For motion of the walkers within Φ_1, we need to know the transition rates between configurations $C \sim (i)[j,k]$ and $C' \sim [i,j](k)$. This represents a process in which a walker at i draws a new bond to some site j and then erases the preexisting bond connecting j to k, thus leaving the walker at site k. The detailed balance equation is

$$W^{\text{walk}}_{i\to k} P(j|i)\pi_C = W^{\text{walk}}_{k\to i} P(j|k)\pi_{C'}. \tag{10}$$

The ratio

$$\frac{\pi_{C'}}{\pi_C} = q^{\delta N_l}\frac{h_{ij}}{h_{jk}} \tag{11}$$

depends on $\delta N_l = N_l(C') - N_l(C) = \pm 1$ (or 0 if the moves do not respect a fixed lattice bipartition; see discussion in Sec. II D). As before, we attempt moves according to the distribution $P(j|i) = h_{ij}/H_i$. Then,

$$\delta = \frac{W^{\text{walk}}_{i\to k}}{W^{\text{walk}}_{k\to i}} = \frac{P(j|k)}{P(j|i)}\frac{\pi_{C'}}{\pi_C} = \frac{H_i}{H_k} q^{\pm 1}, \tag{12}$$

which can be solved in the usual way as $W^{\text{walk}}_{i\to k} = \delta/(1+\delta)$ or $W^{\text{walk}}_{i\to k} = \min(1,\delta)$.

Note that the transition rate does not depend on the ratio of bond amplitudes, as it would if we had, for example, selected a site uniformly with $P(j|i) = 1/N$. The ratio h_{ij}/h_{jk} may fluctuate wildly over many orders of magnitude, so subsuming it into the sampling maximizes the efficiency of the algorithm.

In the case of a translationally invariant system, the amplitude for pairing spins at i and j must be a function of the vector $\mathbf{r}_{ij}$ connecting the two sites; i.e., $h_{ij} = h(\mathbf{r}_{ij})$. Hence, $H = \mathsf{H}/N = H_i = \sum_{\mathbf{r}} h(\mathbf{r})$ for all i, which implies that $P(i) = H_i/\mathsf{H} \to 1/N$ is uniform and $P(j|i) = h_{ij}/H_i \to h(\mathbf{r}_{ij})/H$. The algorithm can be summarized as follows:

(1) Pick any valence bond $[i,j]$ (by choosing i uniformly from the set of A sublattice sites and then selecting its partner site in v or v') and break it. The resulting string has endpoints at $\mathbf{R} = \mathbf{r}_i$ and $\mathbf{R}' = \mathbf{r}_j$.

(2) To move the head, choose a new bond vector $\mathbf{r}$ from the distribution $h(\mathbf{r})/H$. So long as $\mathbf{R} + \mathbf{r} \neq \mathbf{R}'$, attempt to draw a new bond from $\mathbf{R}$ to $\mathbf{R} + \mathbf{r} = \mathbf{r}_k$ (for some k). The bond $[k,l]$ that already exists at that site is then erased and the walker is moved to $\mathbf{r}_l$. The move is accepted with probability $\frac{1}{2}$ if its effect is to join another loop to the string and with probability 1 otherwise.

(3) Otherwise, if $\mathbf{R} + \mathbf{r} = \mathbf{R}'$, close the open string by drawing a new valence bond from $\mathbf{R}$ to $\mathbf{R}'$.

The worm algorithm described here is ergodic and guaranteed to have a high acceptance rate. This is in contrast to the original bond-swap scheme proposed in Ref. 29, wherein two A-site or B-site bond endpoints sitting diagonally across a plaquette are swapped using Metropolis sampling. This antiquated algorithm runs into difficulty when the function $h(\mathbf{r})$ is short ranged. In particular, short bonds that are adjacent but not sharing a common plaquette generate long bonds under rearrangement, so whenever the amplitudes for long bonds become small, the acceptance rate can become correspondingly small. Worse, there are typically many trapping configurations from which the simulation can not emerge. The worm algorithm does not suffer from these problems because it can traverse any local barriers by stepping outside the space of closed loops. (We make no claims of novelty in this regard. Other approaches to overcome the sampling difficulty have been presented elsewhere.[37,38,91])

D. Fluctuating sublattice assignment

The discussion in the previous section was specific to the case in which (i) the AB pattern is regular and (ii) the $\mathbf{r}$ vectors that have nonzero $h(\mathbf{r})$ only connect sites in opposite sublattices. If those conditions hold, there are only two possible consequences to the motion of the open string: a loop is joined to the string ($\delta N_l = -1$) or a loop is split off from it ($\delta N_l = +1$). In both cases, represented in Fig. 3 by panels (a)→(b) and (d)→(e), the AB pattern itself is left undisturbed.

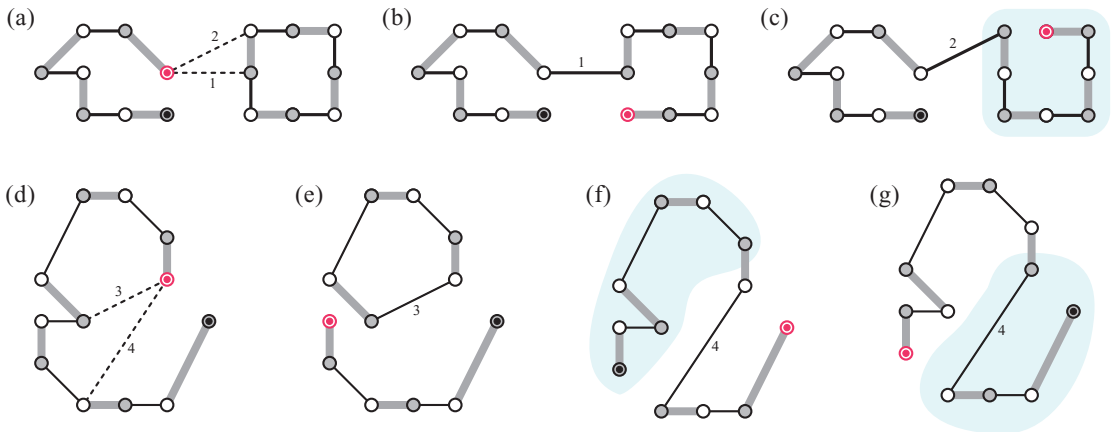

FIG. 3. (Color online) (a) Two possible paths, marked 1 and 2, take the worm head to a site in the opposite or same sublattice of another closed loop. In either case, the loop is absorbed. (b) Path 1 leads to a rearrangement of the worm that preserves the AB labeling. (c) Path 2 requires that the AB labeling be reversed in the highlighted region. (d) Another worm, following two possible paths marked 3 and 4. (e) For path 3, the AB labeling is preserved, and the worm emits a new closed loop. (f),(g) Path 4 requires that the AB labeling be reversed in the highlighted region. The number of loops remains unchanged.

More generally, as the open string propagates, it lays down a chain of singlet bonds whose alternating site labels may be at odds with the traversed sites' current AB assignments. A simple workaround is to flip the sublattice labels as required to correct the mismatch. The relevant processes are now those in which a moving open string absorbs a closed loop ($\delta N_l = -1$) or reorganizes itself without impinging on any additional sites ($\delta N_l = 0$). The first case is depicted in Fig. 3 by panels (a)→(c) and the second by (d)→(f) or (d)→(g). A crucial consideration is that, since the singlets are directional, flipping sublattice labels along a loop segment has the effect of reversing a chain of singlet bonds. If an odd number of singlets is effected, the overall sign of the wave function will change. This is true for all $\delta N_l = 0$ worm steps.

The sublattice mismatch can either be a temporary condition, lasting only until the worm updates succeed in laying down a global AB pattern that is an invariant of the worm motion, or it may be that the motion described by a given $h(\mathbf{r})$ is incompatible with any static AB site labeling. For example, consider the one-parameter family of short-range states on the square lattice described by $h(\pm1,0) = h(0,\pm1) = \cos\theta$ and $h(\pm1,\pm1) = \sin\theta$ (with $0 \leqslant \theta \leqslant \pi/4$). Regardless of the initial sublattice labeling (it can be any random assignment having an equal number of A and B labels), the simulation will dynamically establish the checkerboard pattern provided that $\theta = 0$. We keep track of the AB labeling pattern by measuring a function $\Lambda(\mathbf{Q}) = \sum_{\mathbf{r},\mathbf{r}'} e^{i\mathbf{Q}\cdot(\mathbf{r}-\mathbf{r}')}\langle\langle\lambda(\mathbf{r})\lambda(\mathbf{r}')\rangle\rangle$, where $\lambda(\mathbf{r})$ takes the value -1 or 1 depending on the current sublattice assignment at site $\mathbf{r}$. If $\theta = 0$, $\Lambda(\mathbf{Q})$ starts off broad but systematically flows toward the distribution consisting of a single delta function peak at $\mathbf{Q} = (\pi,\pi)$; once that is achieved, the pattern ceases to evolve. Similar behavior is exhibited at $\theta = \pi/4$, where the system settles into a static pattern with either $\mathbf{Q} = (\pi,0)$ or $\mathbf{Q} = (0,\pi)$. Only in those two extreme cases is the sublattice pattern eventually static and the simulation sign-problem free.

III. RESULTS

As a test of the worm implementation, we compare its output to *analytical* results obtained for the 4×4 lattice. We exploit the fact that the bipartite valence bond basis $\mathcal{V}_{\mathrm{AB}}$ for $2N$ spins is isomorphic to the set of permutations on N elements.[22] Hence, the basis states have a natural lexical ordering via the Lehmer code[92,93] and can easily be enumerated. For $4 \times 4 = 16$ sites, the total number of the states is only $8! = 40\,320$, which means that expectation values of the trial wave function can be evaluated exactly at very little computational cost. Moreover, we can carry out the calculation symbolically. Each observable takes the form of a rational function of order [16/16]:

$$\langle\hat{O}\rangle = \frac{O(x)}{Z(x)} = \frac{3}{4}\frac{\sum_{k=0}^{16} o_k x^k}{\sum_{l=0}^{16} z_l x^l}. \tag{13}$$

The argument of the polynomials appearing in the numerator and denominator is the real-valued ratio $x = h(2,1)/h(1,0)$, and the coefficients o_k and z_k are all integers. Specific values for various observables are listed in Table I.

For this test, we have focused on the nearest- and next-nearest-neighbor spin correlation functions $C_1 = \frac{1}{L^2}\sum_{\langle i,j\rangle}\langle\mathbf{S}_i\cdot\mathbf{S}_j\rangle$ and $C_2 = \frac{1}{L^2}\sum_{\langle\langle i,j\rangle\rangle}\langle\mathbf{S}_i\cdot\mathbf{S}_j\rangle$; the $\mathbf{Q} = (\pi,\pi)$ staggered and $\mathbf{Q} = (\pi,0)$ stripe magnetization, $M^2(\mathbf{Q}) = \frac{1}{L^4}\sum_{\mathbf{r},\mathbf{r}'}(-1)e^{i\mathbf{Q}\cdot(\mathbf{r}-\mathbf{r}')}\langle\mathbf{S}_\mathbf{r}\cdot\mathbf{S}_{\mathbf{r}'}\rangle$; and the order parameter for a columnar dimer crystal $D^2 = \frac{1}{L^4}\sum_{\mathbf{r},\mathbf{r}'}(-1)^{\mathbf{e}_x\cdot(\mathbf{r}+\mathbf{r}')}\langle(\mathbf{S}_\mathbf{r}\cdot\mathbf{S}_{\mathbf{r}+\mathbf{e}_x})(\mathbf{S}_{\mathbf{r}'}\cdot\mathbf{S}_{\mathbf{r}'+\mathbf{e}_x})\rangle$. We have verified that the worm algorithm, conventional bond-swap Monte Carlo, and exact evaluation give consistent results for all these quantities.

TABLE I. The integer coefficients appearing as z_n and o_n in Eq. (13) are presented for various observables. These coefficients specify the rational polynomials in $x = h(2,1)/h(1,0)$ that arise from taking expectation values with respect to the product amplitude trial state on the square lattice of linear size $L = 4$. The columns correspond to the wave-function normalization, the nearest- and next-nearest-neighbor spin correlations, the staggered and stripe magnetization, and the columnar dimer order parameter (with measurements of both its absolute value and its square).

n	Z	$-L^2\,C_1$	$L^2\,C_2$	$L^4\,M^2(\pi,\pi)$	$L^4\,M^2(\pi,0)$	$L^2\,\lvert D\rvert$	$L^4\,4D^2/3$
0	1 559 232	22 241 280	9 902 080	113 983 488	17 383 424	4 376 064	102 133 760
1	13 008 384	194 568 192	104 726 528	1 117 618 176	139 902 976	28 540 928	645 455 872
2	66 018 816	997 232 640	585 695 232	6 104 383 488	709 410 816	127 591 424	2 844 606 464
3	223 842 816	3 395 051 520	2 137 292 800	21 861 335 040	2 381 496 320	389 861 376	8 395 677 696
4	568 694 016	8 564 477 952	5 689 352 192	57 653 526 528	6 069 354 496	932 687 872	19 758 309 376
5	1 108 661 760	16 547 069 952	11 594 661 888	116 342 292 480	11 792 498 688	1 697 314 816	35 459 866 624
6	1 767 412 224	25 797 685 248	18 932 629 504	189 239 033 856	18 888 998 912	2 580 870 144	53 692 563 456
7	2 302 253 568	32 679 444 480	25 148 850 176	250 229 981 184	24 519 589 888	3 165 620 224	65 523 884 032
8	2 528 419 968	34 418 749 440	27 661 209 600	275 349 995 520	27 030 159 360	3 329 164 288	68 794 482 688
9	2 302 253 568	29 878 050 816	25 148 850 176	250 229 981 184	24 519 589 888	2 857 185 280	58 976 903 168
10	1 767 412 224	21 512 073 216	18 932 629 504	189 239 033 856	18 888 998 912	2 089 987 072	43 192 369 152
11	1 108 661 760	12 538 503 168	11 594 661 888	116 342 292 480	11 792 498 688	1 223 688 192	25 387 999 232
12	568 694 016	5 848 903 680	5 689 352 192	57 653 526 528	6 069 354 496	594 391 040	12 360 392 704
13	223 842 816	2 070 282 240	2 137 292 800	21 861 335 040	2 381 496 320	218 601 472	4 580 990 976
14	66 018 816	528 863 232	585 695 232	6 104 383 488	709 410 816	60 980 224	1 313 734 656
15	13 008 384	84 836 352	104 726 528	1 117 618 176	139 902 976	11 331 584	254 992 384
16	1 559 232	6 254 592	9 902 080	113 983 488	17 383 424	1 074 688	31 887 360

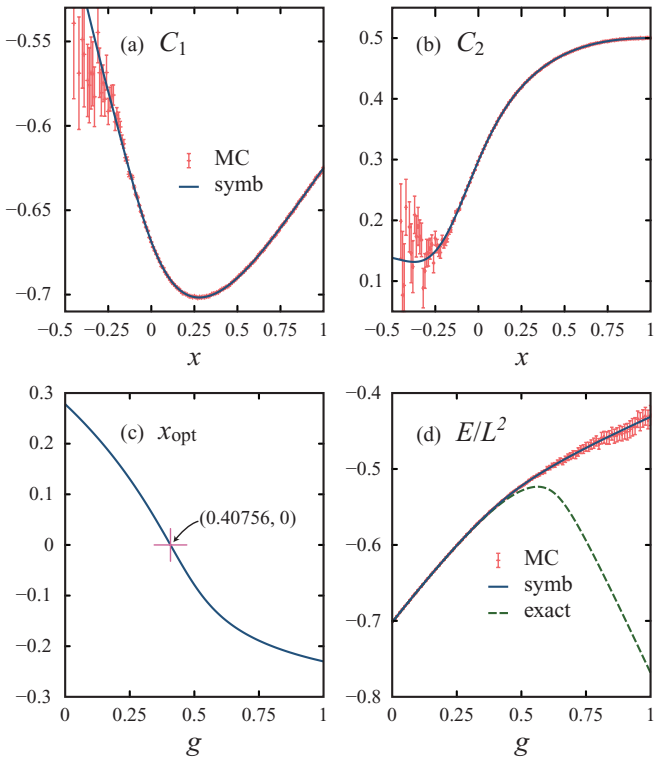

FIG. 4. (Color online) RVB trial wave-function results for the 4×4 lattice. (a), (b) Spin correlations C_1 and C_2 between nearest- and next-nearest-neighbor spins, computed as a function of the amplitude ratio $x = h(2,1)/h(1,0)$. The worm Monte Carlo (MC) results are compared to the corresponding symbolic (symb) expression. As x becomes increasingly negative, the stochastic evaluation becomes dominated by noise from the sign problem. (c) The energy-optimized value x_{opt} remains positive up to $g = J_2/J_1 = 0.40756$. (d) The optimized trial state gives a good approximation to the true ground-state energy (exact) up to where the Marshall sign rule breaks down.

The comparison of the energetics is shown in Fig. 4. Note that in Figs. 4(a) and 4(b), the stochastic evaluation of C_1 and C_2 continues to work in some range of $x < 0$ but breaks down as x becomes strongly negative. For the symbolic result, the determination of the best energy is carried out by considering the two-parameter function $\mathcal{E}(x,g)/J_1L^2 = C_1(x) + gC_2(x)$, which is known exactly by way of Eq. (13). For every value of the relative coupling strength g, the optimal value of x [Fig. 4(c)] is the one that produces the lowest energy [Fig. 4(d)] according to

$$E(g) = \mathcal{E}(x_{opt},g) = \min_x \mathcal{E}(x,g). \tag{14}$$

In practice, Eq. (14) represents a root-finding problem in x for $\partial\mathcal{E}(x,g)/\partial x = 0$; this is solved via Newton-Raphson. We find that the optimized value x_{opt} is positive for weak frustration. It decreases monotonically from its nonfrustrated value $x_{opt} = 0.278\,013\,851\,9$, and drops below zero when the coupling strength exceeds $g = 0.407\,56$. This marks the point at which the Marshall sign rule first fails. For reference (it may be of use in benchmarking RVB calculations accomplished by other methods, e.g., Ref. 94), we report that the specific values $x_{opt} = 0.006\,787\,458\,952$, $-0.037\,771\,217\,11$, $-0.078\,810\,726\,79$, and $-0.112\,818\,471\,1$ obtain at coupling strengths $g = 0.40$, 0.45, 0.50, and 0.55.

Having established confidence in our numerical implementation, we proceed with unbiased optimization calculations using a static sublattice assignment on lattices up to size $L = 32$. Convergence is limited by statistical uncertainty in the (energy to bond count) correlation function that determines the local energy gradient,[34] and it is difficult to optimize reliably for larger system sizes. (See Appendix A for more details.) We first consider the checkerboard AB pattern. At $g = 0$, the bond amplitudes are given an initial value

$$h(x,y) = [\min(x,L-x)^2 + \min(y,L-y)^2]^{-3/2} \tag{15}$$

for $|x| + |y|$ odd and zero otherwise. The new set of amplitudes obtained from this first run serves as the input for the next optimization process. That is to say, we daisy chain the calculations, at each step using the converged result at g to seed the simulation at $g + \delta g$. An analogous procedure is carried out for the stripe AB pattern, starting from $g = \infty$ and stepping the relative coupling down.

One finds that the two sets of simulations do not join smoothly but instead meet with strongly opposite slopes dE/dg. A careful extrapolation to the thermodynamic limit, presented in Fig. 5, puts the location of the energy-level crossing at $g_{c2} \doteq 0.5891(3)$. As Fig. 6 makes clear, this point represents the rightmost edge of an intermediate phase that

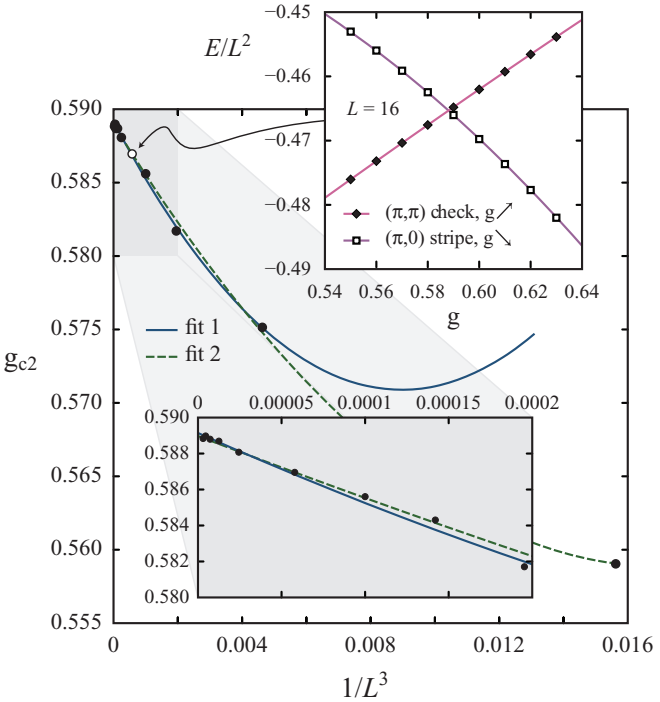

FIG. 5. (Color online) The level crossings are plotted versus $1/L^3$ and extrapolated to the thermodynamic limit. Several different second-order polynomial fits (two shown) are used to estimate the uncertainty in the intercept. The solid blue line (fit 1) is an attempt to fit the $L \geqslant 6$ data to $c_0 \exp(c_1L^{-3} + c_2L^{-6})$; the dashed green line (fit 2) is a fit to $c_0 + c_1L^{-3} + c_2L^{-6}$ for $L \geqslant 4$. Our analysis suggests a value $g_{c2} \doteq 0.5891(3)$. The upper inset shows the analysis behind the $L = 16$ data point, which is marked in the main graph as an open circle. The lower inset is a magnification of the shaded region.

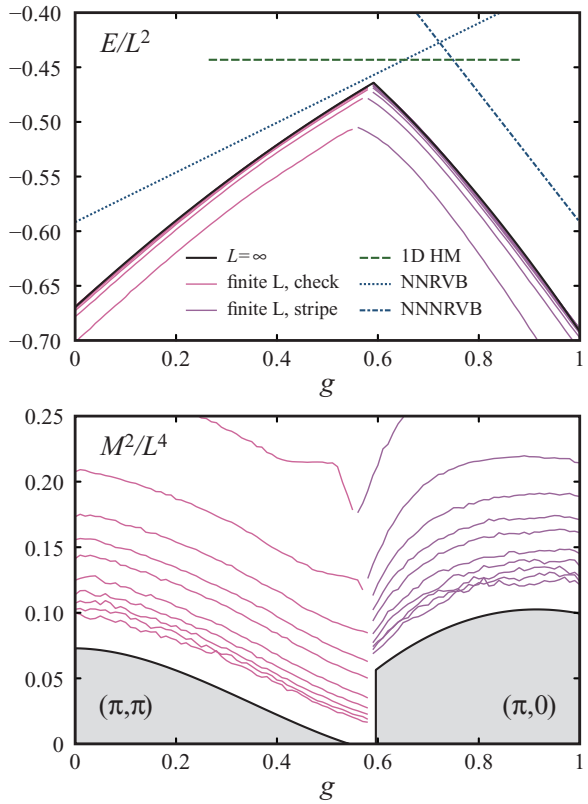

FIG. 6. (Color online) (Upper panel) The energy per site versus the coupling strength. The solid lines are best energies from the trial wave-function optimization. From bottom to top, system sizes $L = 4,6,8,10,12,16,20,24,28,32$ are shown. The thick black line, providing an upper envelope to the curves, is the extrapolation to $L = \infty$. The ground-state energy of the one-dimensional Heisenberg chain is shown for comparison, as are the energies of the NNRVB state and its 45°-rotated, next-nearest-neighbor analog, the NNNRVB state. (Lower panel) Magnetization data are shown, with the same system sizes now increasing from top to bottom. The thick black lines above the gray shading are the $L = \infty$ extrapolation. The magnetic order for $\mathbf{Q} = (\pi,\pi)$ and $\mathbf{Q} = (\pi,0)$ both vanish in the small region between $g_{c1} \doteq 0.54(1)$ and $g_{c2} \doteq 0.5891(3)$.

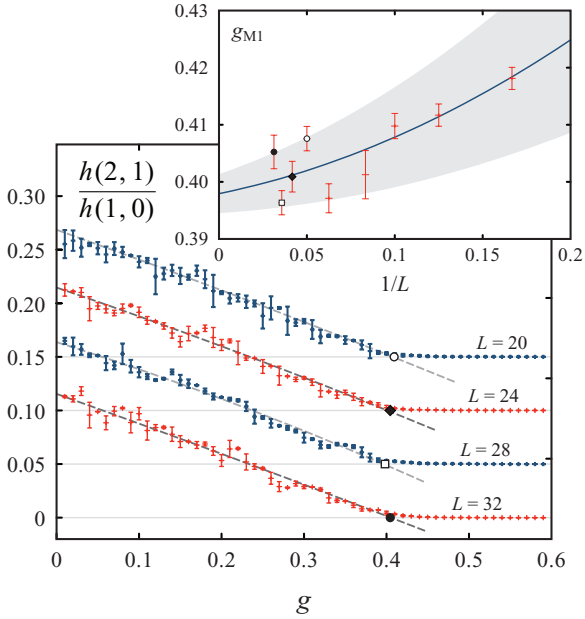

FIG. 7. (Color online) (Main panel) The knight's move amplitude measured relative to the nearest-neighbor bond amplitude, offset vertically by $0.05 \times (8 - L/4)$ to aid viewing, decreases as a function of g. (Inset) The coupling strength at which $h(2,1)$ extrapolates to zero is plotted against the inverse linear system size. The point style for each system size matches the intercept in the main panel. The shaded region represents the envelope containing plausible fits. We estimate that the checkerboard Marshall sign rule fails at $g_{M1} \doteq 0.398(4)$ in the thermodynamic limit.

is magnetically disordered. The leftmost edge sits at $g_{c1} \doteq 0.54(1)$, where the $\mathbf{Q} = (\pi,\pi)$ antiferromagnetism vanishes in a continuous fashion. As a rough gauge of the quality of the RVB trial wave function, we note that for $g = 0.5$ the energy density extrapolates to $E_{RVB} = -0.490\,23(2)$ in the thermodynamic limit. This result is bracketed by the energies of the best projected entangled pair states (PEPS) with bond dimension $D = 3$ [$E_{PEPS} = -0.486\,12(2)$; see Ref. 94] and $D = 9$ [$E_{PEPS} = -0.4943(7)$; see Ref. 75].

An important detail is that the optimizations are carried out with the bond amplitudes constrained to have x- and y-axis reflection symmetry but not necessarily 90° rotation symmetry. In the case of the checkerboard simulation, the amplitudes nonetheless realize the full lattice symmetry under optimization up to large values of the relative coupling. For small lattice sizes $L = 4,6,8$, the symmetry breaks down beyond values $g \approx 0.51,0.55,0.57$. For all larger sizes, that point is pushed well to the right of g_{c2}. This means that, in the thermodynamic limit, $h(\mathbf{r})$ shares a common symmetry across both the staggered magnetic phase and the disordered intermediate phase. But, it experiences a sudden break at the onset of stripe magnetic order, dropping from C_4 to C_2.

In the vicinity of $g = 0$, the optimized bond amplitudes are positive definite and an almost perfect function of bond length. As the frustration increases, the amplitudes begin to deviate from circular symmetry, developing strong lobes of weight along the x and y axes. Bonds not aligned along those preferred directions become increasingly short ranged, and the eight knight's move bonds, those symmetry equivalent to $h(2,1)$, eventually trend through zero to negative values. The extrapolation shown in Fig. 7 pinpoints the breakdown of the Marshall sign rule at $g_{M1} \doteq 0.398(4)$. What this suggests is that there is strict adherence to a checkerboard Marshall sign rule only below g_{M1}; in the range $g_{M1} < g < g_{c2}$, the sign rule is violated, even though the overall sign structure is still partially consistent with the checkerboard pattern. [There is no indication that the amplitudes of any other bond type are on track to change sign. Attempts to extrapolate the amplitudes next most likely to turn negative, viz. $h(4,1)$ and $h(6,1)$, put their vanishing points deep in the intermediate phase or beyond it.] We find that the behavior on the large coupling side is not comparable. There, the coupling at which bond amplitudes first go negative scales as $g_{M2} \sim L^4$ and hence does not converge in the thermodynamic limit. We interpret this to mean that the static stripe pattern is only ever a weak description of the Marshall sign structure (see Fig. 8).

We have attempted to confirm this picture by running simulations in which the Marshall sign structure is determined

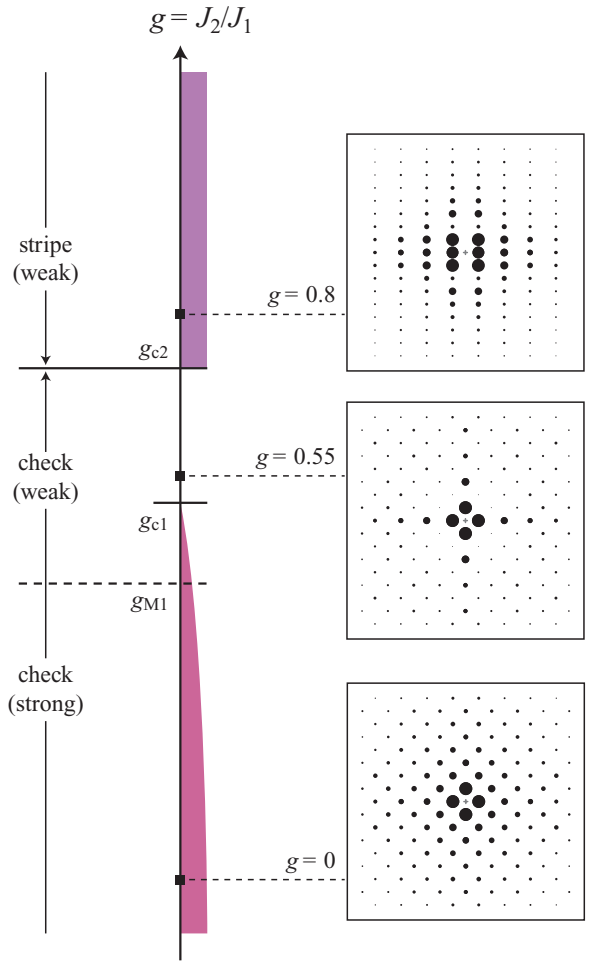

FIG. 8. (Color online) Schematic representation of the model's zero-temperature phase diagram. Critical couplings g_{c1} and g_{c2} mark the boundaries of the magnetically disordered phase. Staggered order ends with a continuous transition at g_{c1}; stripe order ends with a first-order transition at g_{c2}. The three diagrams on the right illustrate the optimized $h(\mathbf{r})$ values at $g = 0$, $g = 0.55$, and $g = 0.8$. Each circle, offset by a vector $\mathbf{r}$ (measured from the small cross at the center), has an area proportional to the corresponding $h(\mathbf{r})$ value. The text on the left describes the Marshall sign structure that predominates.

dynamically. More specifically, we want to verify that the strongly first-order transition at g_{c2} is not merely an artifact of two static, incompatible sublattice conventions colliding. And, we would like to see if any pattern other than checkerboard or stripe could emerge on its own. If permitted, might the system's sublattice structure smoothly interpolate over some range of g, with the peak in $\Lambda(\mathbf{Q})$ migrating from (π,π) to $(\pi,0)$? Or, perhaps with the peak in $\Lambda(\mathbf{Q})$ broadening into incoherence? We follow the procedure outlined in Sec. II D, whereby the sublattice labeling is no longer fixed and the worm motion itself is allowed to reconfigure the current AB pattern. Our approach is to simulate for various g values, with *no* daisy chaining, in each case starting from a random AB pattern and a random loop configuration. The bond amplitudes are initialized with $h(\mathbf{r})$ forming a broad peak around $\mathbf{r} = \mathbf{0}$ and having no zero entries. We perform a crude simulation in which the signs associated with the worm updates are thrown away (see Appendix B). Otherwise, the optimization of $h(\mathbf{r})$ proceeds as before. What we find is a result that exactly tracks the state of lower energy produced by assuming one of the two static AB patterns. The simulation flows to the checkerboard for all $g < g_{c2}$ and to the stripe for all $g > g_{c2}$; the peak in $\Lambda(\mathbf{Q})$ jumps discontinuously. Obviously, we should not read too much into a result that follows from an uncontrolled approximation (sampling by ignoring the signs), but it does give us a sense that the stability of the checkerboard pattern through the intermediate phase and the abrupt change in Marshall sign structure at g_{c2} might be genuine features of the model.

The optimized state in the intermediate phase is definitely not a bond crystal. For a given lattice, the dimer correlations are somewhat enhanced in the strongly frustrated region, but with

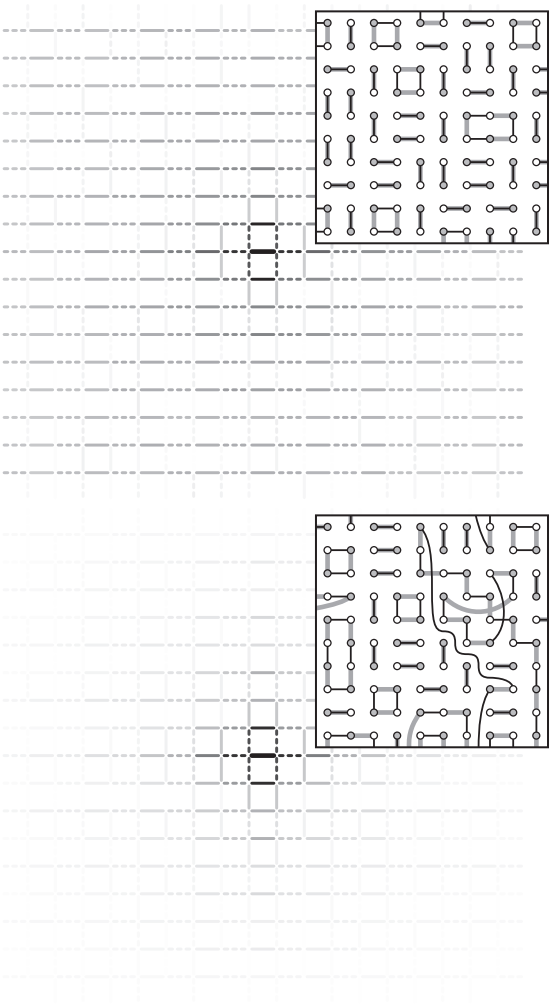

FIG. 9. Grid lines depict the dimer correlations $C_{ijkl} = \langle(\mathbf{S}_i \cdot \mathbf{S}_j)(\mathbf{S}_k \cdot \mathbf{S}_l)\rangle$ on the nearest-neighbor links (k,l) of the square lattice, measured with respect to the thick, dark dimer (i,j) at the center. The correlations are computed for the $L = 28$ system. The grayscale intensity represents correlation strength, presented as the fourth power of $(1 + \frac{3}{2} r_{ij;kl}^{3/2}) C_{ijkl}$, where $r_{ij;kl}$ is the distance measured from the center of the (i,j) bond to the center of the (k,l) bond. Dotted lines indicate a negative (anticorrelated) value. The top panel shows results for the NNRVB state, presented for comparison's sake. The bottom panel shows results for the energy-optimized state at $g = 0.58$. In each case, a 10×10 section of the full valence bond loop configuration, obtained from a snapshot of the Monte Carlo simulation, is overlaid.

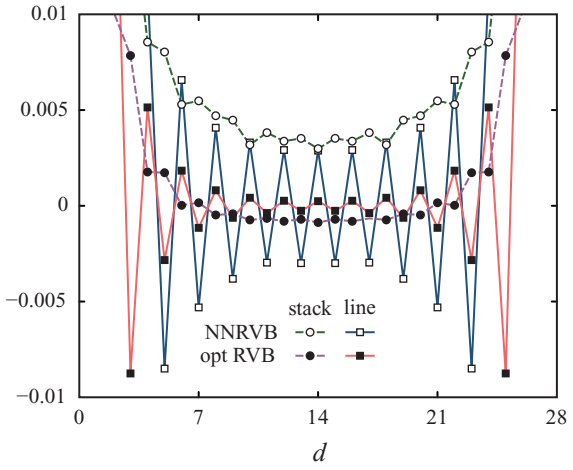

FIG. 10. (Color online) Dimer correlations of the product-amplitude trial wave function optimized at $g = 0.58$ (solid points) and the short-bond-only RVB state (open points) are compared on the $L = 28$ lattice. Presented are the dimer line (squares) and dimer stack (circles) correlation functions. See Eq. (16) and accompanying text for definitions.

increasing lattice size they show clear convergence to zero. Still, spatially resolved dimer correlations do give us important information. One can see in Fig. 9 that the optimized state shows the same pattern of dimer correlation and anticorrelation as the NNRVB, but it decays much faster as a function of dimer separation. The comparison is made more explicit in Fig. 10, which shows correlations along a line and a stack of dimers. The functions measured are

$$\begin{aligned} C_{\text{line}}(d) &= \langle \hat{B}(0,0)\hat{B}(d,0)\rangle - \langle \hat{B}(0,0)\rangle\langle \hat{B}(d,0)\rangle, \\ C_{\text{stack}}(d) &= \langle \hat{B}(0,0)\hat{B}(0,d)\rangle - \langle \hat{B}(0,0)\rangle\langle \hat{B}(0,d)\rangle, \end{aligned} \tag{16}$$

which we have expressed in terms of the x-directed bond operator $\hat{B}(x,y) = \mathbf{S}(x,y)\cdot\mathbf{S}(x+1,y)$.

IV. CONCLUSIONS

We have used an optimized valence bond trial wave function to study the square-lattice J_1-J_2 Heisenberg model, with an eye to both mapping out the zero-temperature phase diagram and determining how the Marshall sign structure breaks down near the phase boundaries. In the first instance, we fix the AB sublattice labeling to coincide with the order that exists at small and large coupling. For each lattice size, the intermediate phase is approached in two independent simulations (or, rather, chains of history-dependent simulations) by evolving the states progressively out of the two ordered phases, minimizing their energy at each step. These simulations are fully non-sign-problematic since the AB pattern is fixed and the bond amplitudes are restricted to be positive.

Finite-size scaling of the dimer order parameter suggests that there is no long-range dimer order at any value of g. This is as expected since the trial state explicitly ignores bond-bond correlations beyond those generated by the hard-core tiling constraint. Measurements of the staggered magnetization show clear evidence of a continuous phase transition in which the staggered magnetization vanishes at $g_{c1} \doteq 0.54(1)$. On the other edge of the intermediate phase, an energy-level crossing at $g_{c2} \doteq 0.5891(3)$ results in the sudden disappearance of the otherwise robust stripe magnetization. This is accompanied by the restoration of the system's rotational symmetry. [Since the trial state is least able to describe the intermediate phase (again, because of its lack of explicit bond-bond correlations) we should probably view g_{c1} and g_{c2} as upper and lower bounds, respectively, on the true positions of the phase boundaries.] We have also performed calculations (approximate and uncontrolled, but suggestive) in which no sublattice labeling is put in by hand and the AB pattern is allowed to emerge dynamically. We find that, regardless of the initial sublattice assignment, the simulation reliably settles into the checkerboard pattern for all $g < g_{c2}$ and the stripe for all $g > g_{c2}$. Taken together, our results point to the checkerboard AB pattern being the best choice throughout the intermediate phase. Hence, within the context of our particular trial wave-function scheme, we surmise that the state beyond g_{c1} is a "bosonic" spin liquid with the lowest-lying magnetic excitations at (π,π).

Figure 8 gives a quick summary of our results. We observe that at high frustration the bond amplitudes take on a highly anisotropic form. This is quite different from the long-bond to short-bond picture that is usually invoked. Recall that Liang, Ducot, and Anderson studied long-range RVB states on the square lattice with amplitudes $h \sim r^{-p}$ that decay as a power law in the bond length r.[29] In that framework, the state becomes magnetically disordered when p exceeds a critical value of 3.3,[31,95,96] and the entire family of states in the range $p > 3.3$ is continuously connected to $p = \infty$, which is the (short-bond-only) NNRVB. The intermediate phase state obtained in our simulations is of a quite different character: (i) the state is magnetically disordered not because its bond amplitudes are uniformly short ranged but because they have become short ranged over some sufficiently large angular interval of bond orientation; (ii) its spin and dimer correlations are distinct from those of the NNRVB; and (iii) the presence of many system-spanning bonds implies that the usual topological invariant for short-ranged RVB states, defined by the parity of bond cuts along a reference line,[7,37] is almost certainly not a good quantum number.

ACKNOWLEDGMENTS

This work was supported by a Discovery grant from NSERC of Canada.

APPENDIX A: NUMERICAL OPTIMIZATION OF THE RVB BOND AMPLITUDES

The RVB ansatz assumes that the quantum amplitude $\psi(v)$ associated with each valence bond state $|v\rangle$ is of the factorizable form

$$\psi(v) \approx \prod_{[i,j]\in v} h(\mathbf{r}_{ij}) \equiv \prod_{\tilde{\mathbf{r}}} h(\tilde{\mathbf{r}})^{n(\tilde{\mathbf{r}};v)}. \tag{A1}$$

The first product ranges over all pairs of spins forming a singlet bond. The second ranges over the minimal set of vectors $\tilde{\mathbf{r}}$ that are inequivalent under whatever lattice symmetries have been enforced. The whole-number exponent $n(\tilde{\mathbf{r}};v)$ represents how many times a bond amplitude $h(\mathbf{r})$, with $\mathbf{r}$ symmetry

equivalent to $\tilde{\mathbf{r}}$, appears in the product for a given v. [Hence, $\sum_{\tilde{\mathbf{r}}} n(\tilde{\mathbf{r}}) = L^2/2 = N$, the number of bonds appearing in $|v\rangle$.]

Accordingly, the energy expectation value is

$$E = \frac{\langle\psi|\hat{H}|\psi\rangle}{\langle\psi|\psi\rangle} = \frac{\sum_C H(C)w(C)}{\sum_C w(C)} \equiv \langle\langle H\rangle\rangle, \tag{A2}$$

where $H(C) = \langle v|\hat{H}|v'\rangle/\langle v|v'\rangle$ is the loop estimator of the Hamiltonian. The notation $\langle\langle\cdots\rangle\rangle$ denotes averaging with respect to the Monte Carlo weight

$$w(C) = \langle v|v'\rangle\psi(v)\psi(v') = \pm q^{N_l(C)} \prod_{\tilde{\mathbf{r}}} h(\tilde{\mathbf{r}})^{n(\tilde{\mathbf{r}};C)}. \tag{A3}$$

Here, each configuration $C = (v, v')$ is a superposition of two dimer coverings, and the sum $n(\tilde{\mathbf{r}}; C) \equiv n(\tilde{\mathbf{r}}; v) + n(\tilde{\mathbf{r}}; v')$ is the combined count of $\tilde{\mathbf{r}}$-type bonds in states $|v\rangle$ and $|v'\rangle$. The $\pm$ on the right-hand side of Eq. (A2) acknowledges that the configuration weight may be negative if the sublattice pattern is not fixed. By way of the identity

$$\frac{\partial w(C)}{\partial h(\tilde{\mathbf{r}})} = \frac{n(\tilde{\mathbf{r}}; C)w(C)}{h(\tilde{\mathbf{r}})}, \tag{A4}$$

we find that the downhill direction in the energy landscape parametrized by $\{h(\tilde{\mathbf{r}})\}$ is related to the energy to bond count correlation function

$$G_k(\tilde{\mathbf{r}}) \equiv -\frac{\partial E}{\partial \ln h(\tilde{\mathbf{r}})} = \langle\langle H\rangle\rangle_k \langle\langle n(\tilde{\mathbf{r}})\rangle\rangle_k - \langle\langle Hn(\tilde{\mathbf{r}})\rangle\rangle_k. \tag{A5}$$

In anticipation of Eq. (A6), we have used $\langle\langle\ldots\rangle\rangle_k$ to denote averaging with respect to the kth Monte Carlo bin.

Our optimization procedure is carried out as follows. For a given logarithmic amplitude $\lambda^{(1)} = \ln h(\tilde{\mathbf{r}})$, we generate a sequence of (not always energy-reducing) steps

$$\lambda^{(k+1)} := \frac{\lambda^{(k)} R\,\delta\lambda}{k^{1/3}} \operatorname{sgn} G_k. \tag{A6}$$

R is a random number chosen from the uniform distribution on the interval $[0,1]$, and $k = 1,2,\ldots,1000$ counts the steps taken through the landscape. The $\frac{1}{3}$ power ensures that the step-size envelope decreases by a factor 10 over the course of 1000 steps. The optimization is run repeatedly with restarts for step sizes beginning at $\delta\lambda = 0.1$ and reduced by successive powers of two until convergence is achieved.

The most serious difficulty is that the correlation function estimates $G_k(\tilde{\mathbf{r}})$ become increasingly noisy for large system sizes, to the point where the determination of $\operatorname{sgn} G_k(\tilde{\mathbf{r}})$ is no longer reliable. The problem is most acute for the longest bonds, which appear least frequently and thus have the worst statistics. (The bond amplitudes, which represent the probability of a given type of bond appearing during the Monte Carlo sampling, fall off rapidly as a function of bond length.)

In small amounts, this noise does not interfere with the energy optimization. It simply overlays a randomizing motion, somewhat akin to the effect of nonzero temperature in simulated annealing. Nonetheless, good convergence requires that the noise fall below a certain threshold (set by the depth and curvature of the well in which the energy minimum sits.) In practice, mitigating the noise means taking the Monte Carlo bin size large enough so that the longest bonds in the system (with length $|\tilde{\mathbf{r}}| \sim L$) appear often enough in the sampling. This consideration sets the limit on the systems sizes we can optimize.

APPENDIX B: SIGN-PROBLEMATIC SIMULATIONS

The energy computed by ignoring signs [i.e., by sampling with respect to the *magnitude* of Eq. (A3)] is

$$E^\star = \frac{\sum_C H(C)|w(C)|}{\sum_C |w(C)|} \equiv [\![H]\!]. \tag{B1}$$

Making the substitution $w = |w|\operatorname{sgn} w$, we can rewrite Eq. (A2) as the ratio of averages

$$E = \frac{\sum_C H(C)|w(C)|\operatorname{sgn} w(C)}{\sum_C |w(C)|\operatorname{sgn} w(C)} \equiv \frac{[\![H\operatorname{sgn} w]\!]}{[\![\operatorname{sgn} w]\!]}; \tag{B2}$$

hence, the energy discrepancy $\Delta E = E^\star - E$ takes the form of a correlation function

$$\Delta E = E^\star - E = \frac{[\![H]\!]\cdot[\![\operatorname{sgn} w]\!] - [\![H\operatorname{sgn} w]\!]}{[\![\operatorname{sgn} w]\!]}. \tag{B3}$$

If the $\operatorname{sgn} w$ term fluctuates within the simulation so that $[\![\operatorname{sgn} w]\!] \approx 0$, evaluation of ΔE is impossible due to large statistical uncertainties. Despite this, the actual value of ΔE may itself be small if there is only a weak correlation between the sign and the energy estimator. Moreover, ΔE is identically zero if the $h(\mathbf{r})$ values evolve to produce a static sublattice labeling. So, at the very least, we can view as a rigorous result the fact that no new static pattern emerged over the course of our simulations.

*kbeach@ualberta.ca

[1] A. H. MacDonald, S. M. Girvin, and D. Yoshioka, Phys. Rev. B **37**, 9753 (1988); **41**, 2565 (1990).

[2] S. Fujimoto, Phys. Rev. B **72**, 024429 (2005).

[3] A. Läuchli, J. C. Domenge, C. Lhuillier, P. Sindzingre, and M. Troyer, Phys. Rev. Lett. **95**, 137206 (2005).

[4] A. W. Sandvik, Phys. Rev. Lett. **98**, 227202 (2007).

[5] K. S. D. Beach and A. W. Sandvik, Phys. Rev. Lett. **99**, 047202 (2007).

[6] K. Majumdar, D. Furton, and G. S. Uhrig, Phys. Rev. B **85**, 144420 (2012).

[7] *Frustrated Spin Systems*, edited by H. T. Diep (World-Scientific, Singapore, 2005).

[8] *Introduction to Frustrated Magnetism: Materials, Experiments, Theory*, Springer Series in Solid-State Sciences, Vol. 164, edited by C. Lacroix, P. Mendels, and F. Mila (Springer, Berlin, 2011).

[9] P. W. Anderson, Mater. Res. Bull. **8**, 153 (1973).

[10] I. Affleck and J. B. Marston, Phys. Rev. B **37**, 3774 (1988).

[11] N. Read and S. Sachdev, Phys. Rev. Lett. **62**, 1694 (1989).

[12] G. Misguich, C. Lhuillier, M. Mambrini, and P. Sindzingre, Eur. Phys. J. B **26**, 167 (2002).

[13] M. B. Hastings, Phys. Rev. B **69**, 104431 (2004).

[14]W. Marshall, Proc. R. Soc. Lond. A **232**, 48 (1955).
[15]B. B. Beard and U.-J. Wiese, Phys. Rev. Lett. **77**, 5130 (1996).
[16]O. F. Syljuåsen and A. W. Sandvik, Phys. Rev. E **66**, 046701 (2002).
[17]H. G. Evertz, Adv. Phys. **52**, 1 (2003).
[18]G. Rumer, Göttingen Nachr. Tech. **1932**, 377 (1932).
[19]L. Pauling, J. Chem. Phys. **1**, 280 (1933).
[20]L. Hulthén, Arkiv Mat. Astr. Fysik **26A**, 1 (1938).
[21]P. Fazekas and P. W. Anderson, Philos. Mag. **30**, 23 (1974).
[22]K. S. D. Beach and A. W. Sandvik, Nucl. Phys. B **750**, 142 (2006).
[23]K. S. D. Beach, M. Mambrini, and F. Alet, Phys. Rev. B **77**, 146401 (2008).
[24]S. Liang, Phys. Rev. B **42**, 6555 (1990); **64**, 1597 (1990).
[25]G. Santoro, S. Sorella, L. Guidoni, A. Parola, and E. Tosatti, Phys. Rev. Lett. **83**, 3065 (1999).
[26]A. W. Sandvik, Phys. Rev. Lett. **95**, 207203 (2005).
[27]A. W. Sandvik and H. G. Evertz, Phys. Rev. B **82**, 024407 (2010).
[28]A. Banerjee and K. Damle, J. Stat. Mech. (2010) P08017.
[29]S. Liang, B. Doucot, and P. W. Anderson, Phys. Rev. Lett. **61**, 365 (1988).
[30]Y.-C. Lin, Y. Tang, J. Lou, and A. W. Sandvik, Phys. Rev. B **86**, 144405 (2012).
[31]K. S. D. Beach, arXiv:0707.0297.
[32]In the more familiar spin-wave language, the justification is the weak interaction between magnons at long range; see N. Hasselmann and P. Kopietz, Europhys. Lett. **74**, 1067 (2006).
[33]P. Chandra, P. Coleman, and A. I. Larkin, Phys. Rev. Lett. **64**, 88 (1990).
[34]J. Lou and A. W. Sandvik, Phys. Rev. B **76**, 104432 (2007).
[35]K. S. D. Beach, Phys. Rev. B **79**, 224431 (2009).
[36]J. Richter, N. B. Ivanov, and K. Retzlaff, Europhys. Lett. **25**, 545 (1994).
[37]A. F. Albuquerque and F. Alet, Phys. Rev. B **82**, 180408(R) (2010).
[38]Y. Tang, A. W. Sandvik, and C. L. Henley, Phys. Rev. B **84**, 174427 (2011).
[39]A. Moreo, E. Dagotto, Th. Jolicoeur, and J. Riera, Phys. Rev. B **42**, 6283 (1990).
[40]A. Chubukov, Phys. Rev. B **44**, 392 (1991).
[41]J. Ferrer, Phys. Rev. B **47**, 8769 (1993).
[42]H. A. Ceccatto, C. J. Gazza, and A. E. Trumper, Phys. Rev. B **47**, 12329 (1993).
[43]E. Dagotto and A. Moreo, Phys. Rev. Lett. **63**, 2148 (1989).
[44]H. J. Schulz, T. A. L. Ziman, and D. Poilblanc, J. Phys. I (France) **6**, 675 (1996).
[45]J. Oitmaa and Z. Weihong, Phys. Rev. B **54**, 3022 (1996).
[46]R. F. Bishop, D. J. J. Farnell, and J. B. Parkinson, Phys. Rev. B **58**, 6394 (1998).
[47]R. R. P. Singh, Z. Weihong, C. J. Hamer, and J. Oitmaa, Phys. Rev. B **60**, 7278 (1999).
[48]O. P. Sushkov, J. Oitmaa, and Z. Weihong, Phys. Rev. B **63**, 104420 (2001).
[49]J. Richter and J. Schulenburg, Eur. Phys. J. B **73**, 117 (2010).
[50]J. Reuther and P. Wölfle, Phys. Rev. B **81**, 144410 (2010).
[51]M. P. Gelfand, R. R. P. Singh, and D. A. Huse, Phys. Rev. B **40**, 10801 (1989).
[52]M. P. Gelfand, Phys. Rev. B **42**, 8206 (1990).
[53]R. R. P. Singh and R. Narayanan, Phys. Rev. Lett. **65**, 1072 (1990).
[54]M. E. Zhitomirsky and K. Ueda, Phys. Rev. B **54**, 9007 (1996).
[55]P. W. Leung and N. W. Lam, Phys. Rev. B **53**, 2213 (1996).
[56]V. N. Kotov, J. Oitmaa, O. P. Sushkov, and Z. Weihong, Phys. Rev. B **60**, 14613 (1999).
[57]V. N. Kotov and O. P. Sushkov, Phys. Rev. B **61**, 11820 (2000).
[58]L. Capriotti and S. Sorella, Phys. Rev. Lett. **84**, 3173 (2000).
[59]K. Takano, Y. Kito, Y. Ōno, and K. Sano, Phys. Rev. Lett. **91**, 197202 (2003).
[60]M. Mambrini, A. Läuchli, D. Poilblanc, and F. Mila, Phys. Rev. B **74**, 144422 (2006).
[61]V. Murg, F. Verstraete, and J. I. Cirac, Phys. Rev. B **79**, 195119 (2009).
[62]J. Reuther, P. Wölfle, R. Darradi, W. Brenig, M. Arlego, and J. Richter, Phys. Rev. B **83**, 064416 (2011).
[63]J.-F. Yu and Y.-J. Kao, Phys. Rev. B **85**, 094407 (2012).
[64]L. Capriotti, F. Becca, A. Parola, and S. Sorella, Phys. Rev. Lett. **87**, 097201 (2001).
[65]P. Chandra and B. Doucot, Phys. Rev. B **38**, 9335 (1988).
[66]F. Figueirido, A. Karlhede, S. Kivelson, S. Sondhi, M. Rocek, and D. S. Rokhsar, Phys. Rev. B **41**, 4619 (1990).
[67]T. Oguchi and H. Kitatani, J. Phys. Soc. Jpn. **59**, 3322 (1990).
[68]P. Locher, Phys. Rev. B **41**, 2537 (1990).
[69]H. J. Schulz and T. A. L. Ziman, Europhys. Lett. **18**, 355 (1992).
[70]Q. F. Zhong and S. Sorella, Europhys. Lett. **21**, 629 (1993).
[71]G.-M. Zhang, H. Hu, and L. Yu, Phys. Rev. Lett. **91**, 067201 (2003).
[72]L. Capriotti, F. Becca, A. Parola, and S. Sorella, Phys. Rev. B **67**, 212402 (2003).
[73]L. Capriotti, D. J. Scalapino, and S. R. White, Phys. Rev. Lett. **93**, 177004 (2004).
[74]L. Capriotti and S. Sachdev, Phys. Rev. Lett. **93**, 257206 (2004).
[75]L. Wang, Z.-C. Gu, X.-G. Wen, and F. Verstraete, arXiv:1112.3331.
[76]H.-C. Jiang, H. Yao, and L. Balents, Phys. Rev. B **86**, 024424 (2012).
[77]F. Mezzacapo, Phys. Rev. B **86**, 045115 (2012).
[78]A. W. Sandvik, Phys. Rev. B **85**, 134407 (2012).
[79]M. S. Block and R. K. Kaul, Phys. Rev. B **86**, 134408 (2012).
[80]R. K. Kaul, R. G. Melko, and A. W. Sandvik, Annu. Rev. Condens. Matter Phys. **4**, 179 (2013).
[81]E. Y. Loh Jr., J. E. Gubernatis, R. T. Scalettar, S. R. White, D. J. Scalapino, and R. L. Sugar, Phys. Rev. B **41**, 9301 (1990).
[82]J. Richter, J. Schulenburg, A. Honecker, and D. Schmalfuß, Phys. Rev. B **70**, 174454 (2004).
[83]H. Nakano and T. Sakai, J. Phys. Soc. Jpn. **80**, 053704 (2011).
[84]A. M. Läuchli, J. Sudan, and E. S. Sørensen, Phys. Rev. B **83**, 212401 (2011).
[85]A. Lauchli and R. Johanni, Bull. Am. Phys. Soc. **57**, 1 (2012).
[86]P. W. Anderson, Science **235**, 1196 (1987).
[87]S. Yunoki and S. Sorella, Phys. Rev. Lett. **92**, 157003 (2004).
[88]J. Cano and P. Fendley, Phys. Rev. Lett. **105**, 067205 (2010).
[89]T. Li, F. Becca, W. Hu, and S. Sorella, Phys. Rev. B **86**, 075111 (2012).
[90]N. Prokof'ev and B. Svistunov, Phys. Rev. Lett. **87**, 160601 (2001).
[91]A. W. Sandvik and R. Moessner, Phys. Rev. B **73**, 144504 (2006).
[92]D. H. Lehmer, Proc. Sympos. Appl. Math. **10**, 179 (1960).
[93]D. E. Knuth, *The Art of Computer Programming*, Volume 3: Sorting and Searching (Addison-Wesley, Reading, MA, 1973), p. 12.
[94]L. Wang, D. Poilblac, Z.-C. Gu, X.-G. Wen, and F. Verstraete, arXiv:1112.3331.
[95]M. Havilio and A. Auerbach, Phys. Rev. Lett. **83**, 4848 (1999).
[96]M. Havilio and A. Auerbach, Phys. Rev. B **62**, 324 (2000).